nature climate change

ARTICLES

https://doi.org/10.1038/s41558-020-0815-z

Record warming at the South Pole during the past three decades

Kyle R. Clem[1]✉, Ryan L. Fogt[2], John Turner[3], Benjamin R. Lintner[4], Gareth J. Marshall[3], James R. Miller[4] and James A. Renwick[1]

Over the last three decades, the South Pole has experienced a record-high statistically significant warming of 0.61 ± 0.34 °C per decade, more than three times the global average. Here, we use an ensemble of climate model experiments to show this recent warming lies within the upper bounds of the simulated range of natural variability. The warming resulted from a strong cyclonic anomaly in the Weddell Sea caused by increasing sea surface temperatures in the western tropical Pacific. This circulation, coupled with a positive polarity of the Southern Annular Mode, advected warm and moist air from the South Atlantic into the Antarctic interior. These results underscore the intimate linkage of interior Antarctic climate to tropical variability. Further, this study shows that atmospheric internal variability can induce extreme regional climate change over the Antarctic interior, which has masked any anthropogenic warming signal there during the twenty-first century.

Global mean surface air temperature (SAT) has been increasing since at least the 1880s. Approximately 0.6 °C of warming occurred over the twentieth century (average rate of warming around 0.05 °C decade^{-1}), although the rate of warming has accelerated to 0.15–0.20 °C decade^{-1} since the 1970s[1]. However, substantial spatial heterogeneity exists in climate trends, with regional SAT trends sometimes greatly exceeding, or even opposing, the global mean. These departures from the global-mean trend may signify important regional-scale processes, mechanisms and feedbacks. Since the mid-twentieth century, Antarctica has experienced many of the planet's largest regional temperature trends[2,3]. For example, over the second half of the twentieth century, West Antarctica and the Antarctic Peninsula warmed more than twice as fast as the global average[4–7], but over the first two decades of the twenty-first century, temperature trends there strikingly reversed[8–11]. Such strong regional changes are often most pronounced in the polar regions due to positive ice-albedo feedbacks that amplify warming[5,12], while stratospheric ozone depletion and extreme decadal variability can even induce regional cooling[9,13–15]. In Antarctica, strong fluctuations in SAT occur, in part, because of the continent's sensitivity to tropical forcing[9,16–21], the strength and position of the circumpolar westerly winds[14,22–25], and its exposure to relatively mild and moist oceanic airmass intrusions along its coastline[26–31].

Here, we examine recent SAT changes at Earth's southernmost weather observatory, the Amundsen–Scott station located at the South Pole. An analysis in the 'State of the Climate in 2018'[32] report showed that Amundsen–Scott station (and Vostok, the only other Antarctic Plateau station with a similarly long SAT time series) recorded their warmest year on record in 2018, both being +2.4 °C above their 1981–2010 climatological averages. To place Antarctic climate in the context of increasing global SAT from continuing greenhouse gas forcing, a comprehensive diagnosis of the drivers of such extreme fluctuations in temperature is crucial.

Record warming at the South Pole

The time series of the South Pole annual-mean SAT record (Fig. 1a) and running 30-yr annual-mean SAT trends (Fig. 1b) places 2018 in a historical context. The most recent 30-yr period of 1989–2018 experienced the largest 30-yr annual-mean warming trend on record of 0.61 ± 0.34 °C decade^{-1} (95% confidence interval, CI), over three times the global average rate. Four record-high annual-mean SATs occurred during the twenty-first century (2002, 2009, 2013 and 2018), reflecting a rapid warming coincident with the recent cooling on the Antarctic Peninsula[9]. The recent warming is localized (Extended Data Fig. 1) and it exceeds the continent-wide average warming during the same period by a factor of seven as inferred from 20 staffed and automated weather stations across Antarctica.

Surface warming occurred in every season at the South Pole during the period 1989–2018 (Fig. 1c and Table 1). The strongest warming was in autumn (0.89 ± 0.62 °C) followed by summer and spring (0.62 ± 0.59 °C and 0.61 ± 0.58 °C, respectively); the autumn and summer trends were also record-high 30-yr trends for their respective seasons. Winter is the only season for which the 1989–2018 warming was not significant at $P < 0.05$ (Table 1), while in spring significant warming at $P < 0.10$ is found for all time periods ending after 2014 (Fig. 1c). Mid-tropospheric (500 hPa) geopotential height and temperature at the South Pole have both increased since radiosoundings began in 1961 but neither had significant ($P < 0.10$) trends during the period 1989–2018 (Fig. 1d). In the lower stratosphere (150 hPa), strong cooling and decreasing geopotential height occurred in the earlier part of the record during the period of anthropogenic stratospheric ozone depletion[13,33] but this trend has since weakened and even reversed sign in recent decades (Fig. 1d), likely indicating the onset of ozone hole recovery[34]. Therefore the recent South Pole warming trends are confined to the near-surface, regional and strongest in the last 30 yr.

Circulation changes in the Weddell Sea

To address the source of the recent South Pole warming, we first examine trends in the annual-mean atmospheric circulation (Fig. 2) to relate the South Pole SAT changes with changes in atmospheric flow. There has been a significant ($P < 0.10$) increase in grid northerly wind at the South Pole (Fig. 2a), which is explained via a broad decrease in pressure across the high-latitude South Pacific

[1]School of Geography, Environment and Earth Sciences, Victoria University of Wellington, Wellington, New Zealand. [2]Department of Geography, Ohio University, Athens, OH, USA. [3]British Antarctic Survey, Natural Environment Research Council, Cambridge, UK. [4]Rutgers University, New Brunswick, NJ, USA. ✉e-mail: kyle.clem@vuw.ac.nz

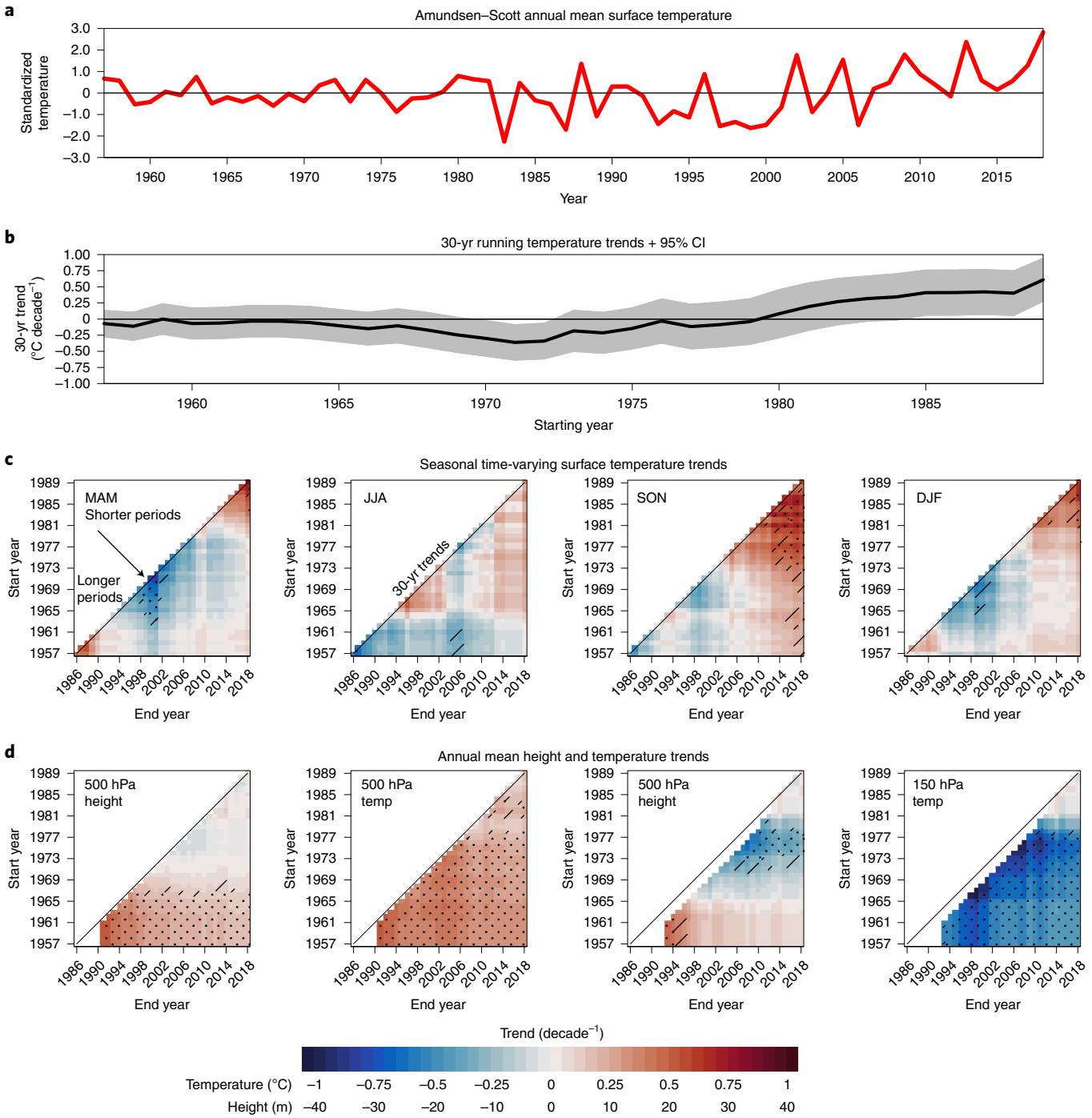

Fig. 1 | Temperature and pressure changes at the South Pole during the modern instrumental record. a,**b**, Time series of the standardized South Pole annual-mean SAT (**a**) and running 30-yr SAT trends (°C decade^{-1}) (**b**), with the 95% CI shaded in grey. **c**,**d**, The time-varying South Pole seasonal-mean SAT trends (**c**) and annual-mean geopotential height and temperature trends at 500 hPa and 150 hPa from South Pole radiosonde data (**d**). In **c** and **d**, the starting year of trend is on the left axis and ending year of trend is on the bottom axis; the $x = y$ axis is exactly 30 yr, and longer periods are in the bottom right corner. Cross-hatching in **c** and **d** indicates trends different from zero at $P < 0.10$ and stippling $P < 0.05$. MAM, March–April–May; JJA, June–July–August; SON, September–October–November; DJF, December–January–February.

and Weddell Sea (significant at $P < 0.10$ over the extreme southwest Weddell Sea) and a slight increase in pressure over the East Antarctic plateau. The circulation trend over the strongest sub-period of South Pole warming 1997–2018 (Fig. 2b) demonstrates the dramatic decrease in pressure in the climatological Amundsen Sea Low, west of the Antarctic Peninsula and in the western Weddell Sea, amplifying the advection of mild, oceanic air from the South Atlantic into the continental interior during the past two decades. These circulation changes are consistent with recent changes in the Weddell Gyre[35], the retreat of sea ice in the Weddell Sea[36] and the twenty-first century cooling on the Antarctic Peninsula[9].

The relationship between observed South Pole wind direction and SAT anomalies is examined in Fig. 2c,d. For all 6-hourly wind reports (Fig. 2c), the winds at the South Pole predominantly originate

Table 1 | The 1989–2018 annual and seasonal-mean linear trends and 95% CI for Amundsen–Scott South Pole SAT, Vostok SAT, SAM index (ref. [46]), ERA5 SAM index (difference in normalized SLP at 40° S and 65° S) and IPO residual index (tripole index after removing covariability with Niño 3.4; see Methods)

	Annual	DJF	MAM	JJA	SON
South Pole	**0.61 ± 0.34**	**0.62 ± 0.59**	**0.89 ± 0.62**	0.35 ± 0.80	**0.61 ± 0.58**
Vostok	0.32 ± 0.47	−0.13 ± 0.72	0.38 ± 0.71	0.08 ± 1.01	**0.93 ± 0.63**
M03 SAM	0.22 ± 0.24	0.20 ± 0.51	0.14 ± 0.38	0.35 ± 0.49	0.17 ± 0.53
ERA5 SAM	0.71 ± 0.78	0.31 ± 0.78	0.52 ± 0.78	0.60 ± 0.81	0.34 ± 0.84
IPO residual	**−0.16 ± 0.08**	**−0.12 ± 0.10**	**−0.13 ± 0.07**	**−0.20 ± 0.11**	**−0.20 ± 0.12**

DJF, December–January–February; MAM, March–April–May; JJA, June–July–August; SON, September–October–November. Units for SAT are °C decade^{-1} and SAM and IPO residual are index decade^{-1}. Trends significant at $P < 0.05$ are boldface.

from 0–90° (that is, from the cold, East Antarctic plateau). For extreme warm SATs that exceed −20 °C (Fig. 2d), winds are mostly from 0° longitude (grid northerly) or grid northwesterly from the Weddell Sea. Considering the percentage of wind directions by decade (Fig. 2e), the 2000s and 2010s have indeed seen an increased frequency of grid northerly to grid northwesterly winds (350° to 20°) relative to earlier decades, reflecting the systematic shift in local wind direction that is consistent with the cyclonic circulation changes in the Weddell Sea.

Internal variability versus anthropogenic forcing

Since the meteorological record at the South Pole is relatively short compared to mid-latitude records (62 yr; Fig. 1a), we next evaluate whether the observed 30-yr warming trend is exceptional when compared to simulated 30-yr South Pole SAT trends in the Coupled Model Intercomparison Project Phase 5 (CMIP5) ensembles (Fig. 3a; Methods). From these large ensembles, the recent 30-yr warming of 1.83 °C lies in the 92nd percentile of all possible simulated 30-yr trends in the anthropogenically forced historical/Representative Concentration Pathway (RCP 8.5) ensemble and the 95th percentile of the unforced pre-industrial ensemble. However, compared to the distribution of highest 30-yr SAT trends simulated in each ensemble member, the observed warming lies only in the 54th and 65th percentile for the historical/RCP 8.5 and pre-industrial ensembles, respectively (not shown). Therefore the recent record warming lies within the range of simulated multi-decadal variability, with and without anthropogenic forcing included.

However, the upper tails of both the pre-industrial and historical/RCP 8.5 ensembles are strongly skewed by one model (Goddard Institute for Space Studies (GISS)), which also has the largest interannual variability. Therefore we evaluate the observed and simulated South Pole SAT trends after normalizing the SAT by interannual variability (Fig. 3a; Methods). First, the distribution of every 30-yr normalized South Pole SAT trend and the distribution of the highest normalized 30-yr trends in each ensemble member, is compared to the observed 1989–2018 normalized SAT trend (left side of Fig. 3a). While the observed trend exceeds the multi-model mean trend in all four distributions, the normalized SAT trend still lies within the simulated range of both forced and unforced normalized variability.

We do note, however, the remarkable nature of the recent observed trend. It lies above 99.9% of all possible normalized trends in both ensembles, and at the 89th and 93rd percentile for the highest normalized trends in the pre-industrial and historical/RCP 8.5 ensembles, respectively. From Extended Data Fig. 2, we estimate the approximate warming due to radiative forcing from the ensemble mean of the historical/RCP 8.5 (Methods) to be 0.98 °C during the 1989–2018 period. However, among the caveats to this estimation of the anthropogenic signal are that externally forced CMIP5 models are known to overestimate Antarctic sea ice loss[37] and therefore SAT warming[38] due to strong ice–ocean–atmosphere feedbacks. Bearing this in mind, given the observed trend is within the upper 0.1% of all simulated trends and the upper 10% of the simulated highest warming trends, and given the model-estimated ~1 °C of warming from radiative forcing, there is reason to expect that the observed trend would not have occurred from unforced variability alone.

To diagnose connections with large-scale climate variability, the right side of Fig. 3a compares the observed 1989–2018 trends in Niño 3.4 sea surface temperature (SST), the Interdecadal Pacific Oscillation (IPO) index and the Southern Annular Mode (SAM) index (Methods) with the distribution of those that occurred in the highest 30-yr warming period for each ensemble member in the pre-industrial simulations. In the models, on-average record South Pole warming is associated with a weak positive SST trend in the Niño 3.4 region (El Niño conditions) and a strong negative trend in the SAM index, consistent with existing knowledge of tropical Pacific and SAM influences on interior Antarctic temperatures[16,17,24,29]. By contrast, the observed 1989–2018 SAM index trend was strongly positive and the IPO index trend was strongly negative, both of which are well outside the simulated distributions. Meanwhile, there was no trend in Niño 3.4 SSTs observed during the period 1989–2018.

Looking spatially at the ensemble mean SST, sea-level pressure (SLP) and SAT 30-yr trends during their highest warming periods (Fig. 3b–d) illustrates the positive SST trend in the central tropical Pacific extends well into the western equatorial Pacific, which is atypical for an El Niño pattern[39,40]. The negative SAM pattern is very pronounced with positive SLP trends over Antarctica and negative SLP trends across Southern Hemisphere mid-latitudes. The SAT warming pattern follows the northwest edge of an anticyclone over the East Antarctic plateau, while there is also a notable minimum in the broader positive SLP trend over the Weddell Sea, which together turn the flow of warm air from the South Atlantic poleward into the continental interior via north-northwesterly geostrophic flow. Since the observed warming is tied to the decrease in pressure in the Weddell Sea, next we compare the observed (ERA5) 1989–2018 SLP trend in the Weddell Sea with the distribution of Weddell Sea SLP trends in the models during their highest warming period (Fig. 3a, far right). The observed deepening of pressure (−1.58 hPa 30-yr^{-1}) is well below the ensemble mean positive trend (+0.36 hPa 30-yr^{-1}) due to the simulated negative SAM pattern; however, it lies well within the model distribution, and in fact 20 of the 52 models (39%) also display a negative SLP trend in the Weddell Sea during their record South Pole warming period consistent with the observed decrease in SLP there.

Connections with tropical variability

In Fig. 4a,c,e, we examine spatial trends for only those 20 models with a negative SLP trend in the Weddell Sea, as these align best with the observed circulation pattern that has warmed the South Pole. These models show a positive SST trend over the central and

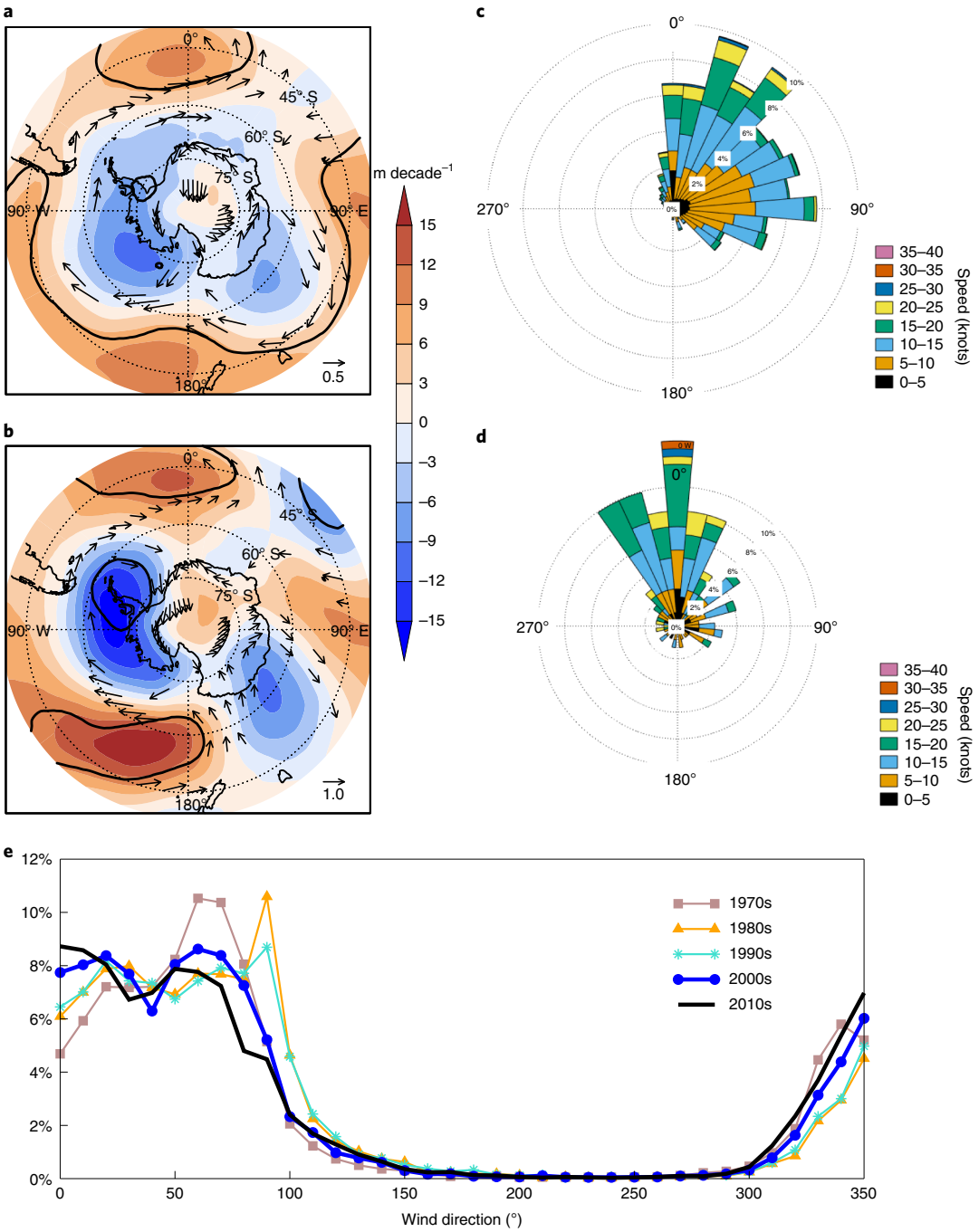

Fig. 2 | Circulation changes at the South Pole and the southern polar region. a,**b**, The annual-mean ERA5 Z500 (m decade^{-1}) and 500 hPa wind (ms^{-1} decade^{-1}) trends for 1989–2018 (**a**) and 1997–2018 (**b**), the latter being the sub-period of strongest annual-mean warming at the South Pole since 1989 (not shown). The black contours in **a** and **b** show where the Z500 trends are significant at $P < 0.10$, and only wind trends significant at $P < 0.10$ are plotted. **c**,**d**, Wind rose for all (1957–2018) six-hourly wind direction observations (90,955 in total) from the South Pole (**c**) and all 'extreme' warm occasions where the South Pole SAT exceeded −20 °C (**d**). **e**, The percentage of South Pole wind directions by decade.

western equatorial Pacific (Fig. 4a) and a pronounced wave train originating from the tropics (Fig. 4c). This points to the potentially important role of tropical Pacific SSTs in generating the cyclonic circulation in the Weddell Sea, and indeed the observed South Pole SAT is strongly positively correlated with western tropical Pacific SSTs (black box in Fig. 4a) at $P < 0.01$ (Extended Data Fig. 3) and, furthermore, during 1989–2018 there was a statistically significant increase in SST and deep convective rainfall ($P < 0.10$) within this region (Extended Data Fig. 4). Note that the west Pacific SST region is not correlated with the El Niño/Southern Oscillation (ENSO) (Methods). Rather, the observed SST increases in the western equatorial Pacific are linearly congruent with the recent negative IPO trend that was significant at $P < 0.05$ in all seasons (Table 1) and exceptional compared to the model distribution (Fig. 4g), as is the observed decrease in SLP over the Bellingshausen and Weddell Seas (Fig. 4h). This is consistent with earlier work[9,11] that related increased cyclonic activity near the Drake Passage with the post−2000 negative IPO phase.

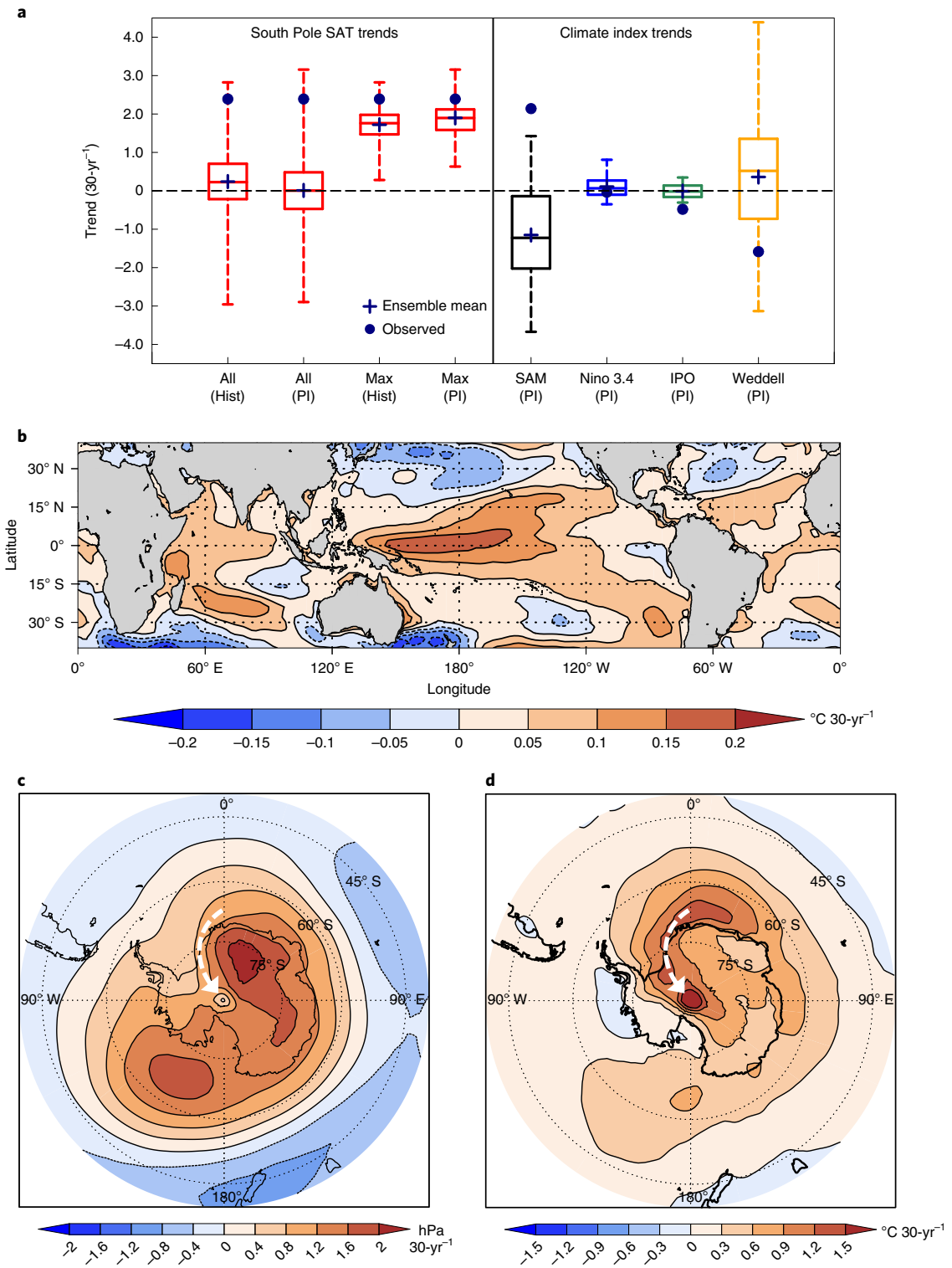

Fig. 3 | Recent South Pole climatic changes relative to CMIP5 ensemble. a, Box and whisker plot showing (left) the distribution of every possible 30-yr annual-mean South Pole normalized SAT trend in the CMIP5 historical (Hist)/RCP 8.5 and pre-industrial (PI) ensembles and the distribution of the highest 30-yr normalized SAT trend in each ensemble member, and (right) the distribution of annual-mean 30-yr trends in the SAM index, Niño 3.4 SST, IPO residual index and SLP averaged over the Weddell Sea (62–72° S, 60–35° W) during each ensemble member's highest 30-yr South Pole warming period in the pre-industrial ensemble. The observed 1989–2018 annual-mean normalized South Pole SAT trend and climate index trends are shown as filled blue circles in **a**. Units in **a** are total 30-yr change in normalized SAT, Niño 3.4 SST (°C), SAM index and SLP (hPa). Whiskers indicate maximum and minimum values, and boxes indicate the 75th and 25th percentiles as well as the median. **b**–**d**, The CMIP5 pre-industrial ensemble mean trend for the 30-yr periods of highest South Pole warming: tropical SST (°C 30-yr^{-1}) (**b**), SLP (hPa 30-yr^{-1}) (**c**) and SAT (°C 30-yr^{-1}) (**d**).

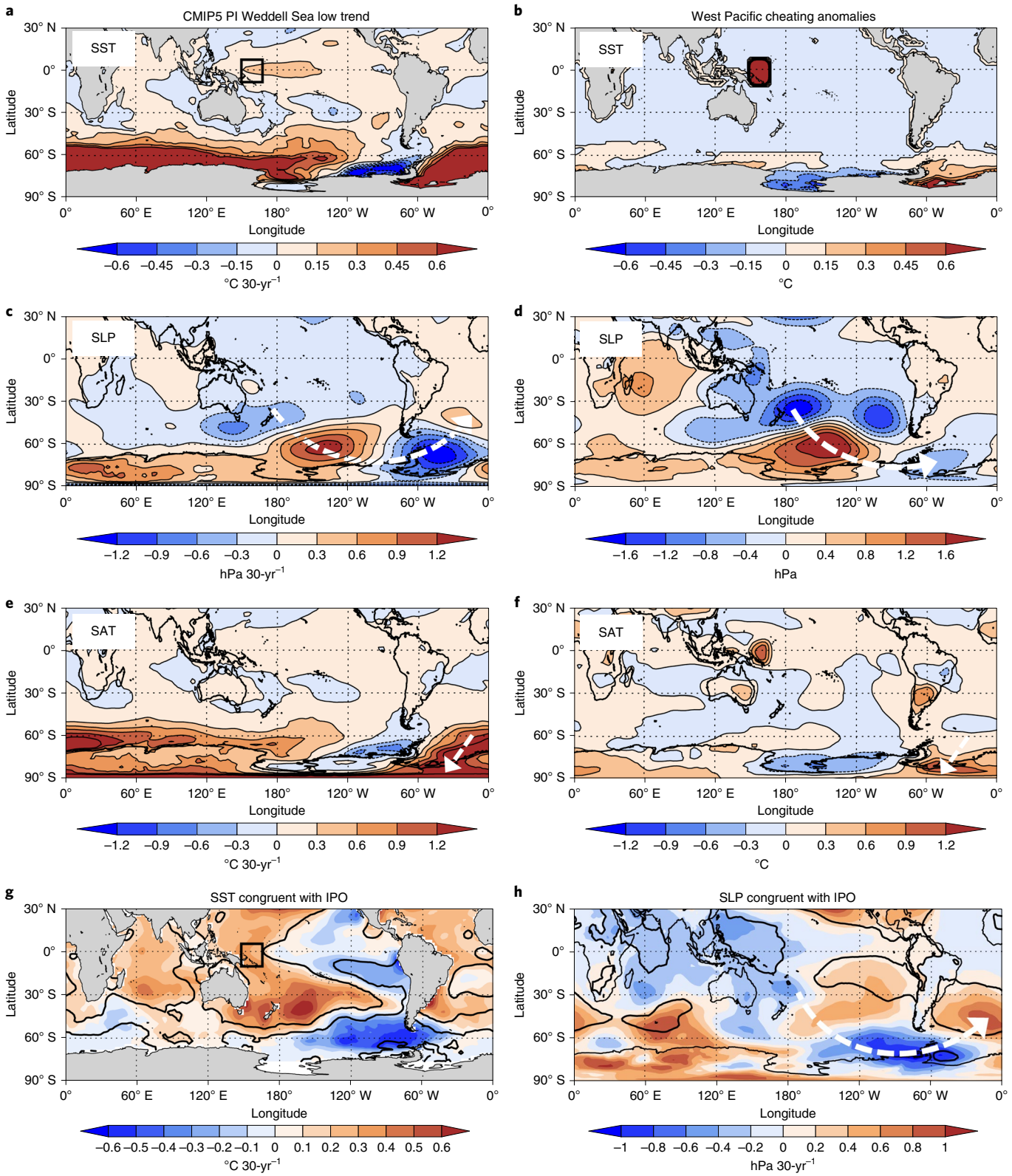

Fig. 4 | Connection to tropical Pacific variability. a,**c**,**e**, The CMIP5 pre-industrial ensemble mean 30-yr trend for the 20 models that had a negative pressure trend in the Weddell Sea during their highest 30-yr South Pole warming period: SST (°C 30-yr^{-1}) (**a**), SLP (hPa 30-yr^{-1}) (**c**) and SAT (°C 30-yr^{-1}) (**e**). **b**,**d**,**f**, The simulated annual-mean anomalies (difference in perturbed minus control runs) for a western equatorial Pacific SST heating anomaly placed at 158° E, 2° S (as denoted by black box in **a**): SST (°C) (**b**), SLP (hPa) (**d**) and SAT (°C) (**f**). In **b**, the red rectangular shape indicates SST anomalies from our sensitivity experiment. **g**,**h**, The annual-mean ERSSTv.5 (°C 30-yr^{-1}) (**g**) and ERA5 SLP (hPa 30-yr^{-1}) (**h**) trends that are linearly congruent with the observed annual-mean 1989–2018 negative IPO residual index trend. The black contours in **g** and **h** show where the IPO residual index correlation with ERSSTv.5 and ERA5 SLP for the period 1979–2018 is statistically significant at $P < 0.10$. The white arrows in **c**–**f** and **h** indicate the wave train emanating from the tropical Pacific.

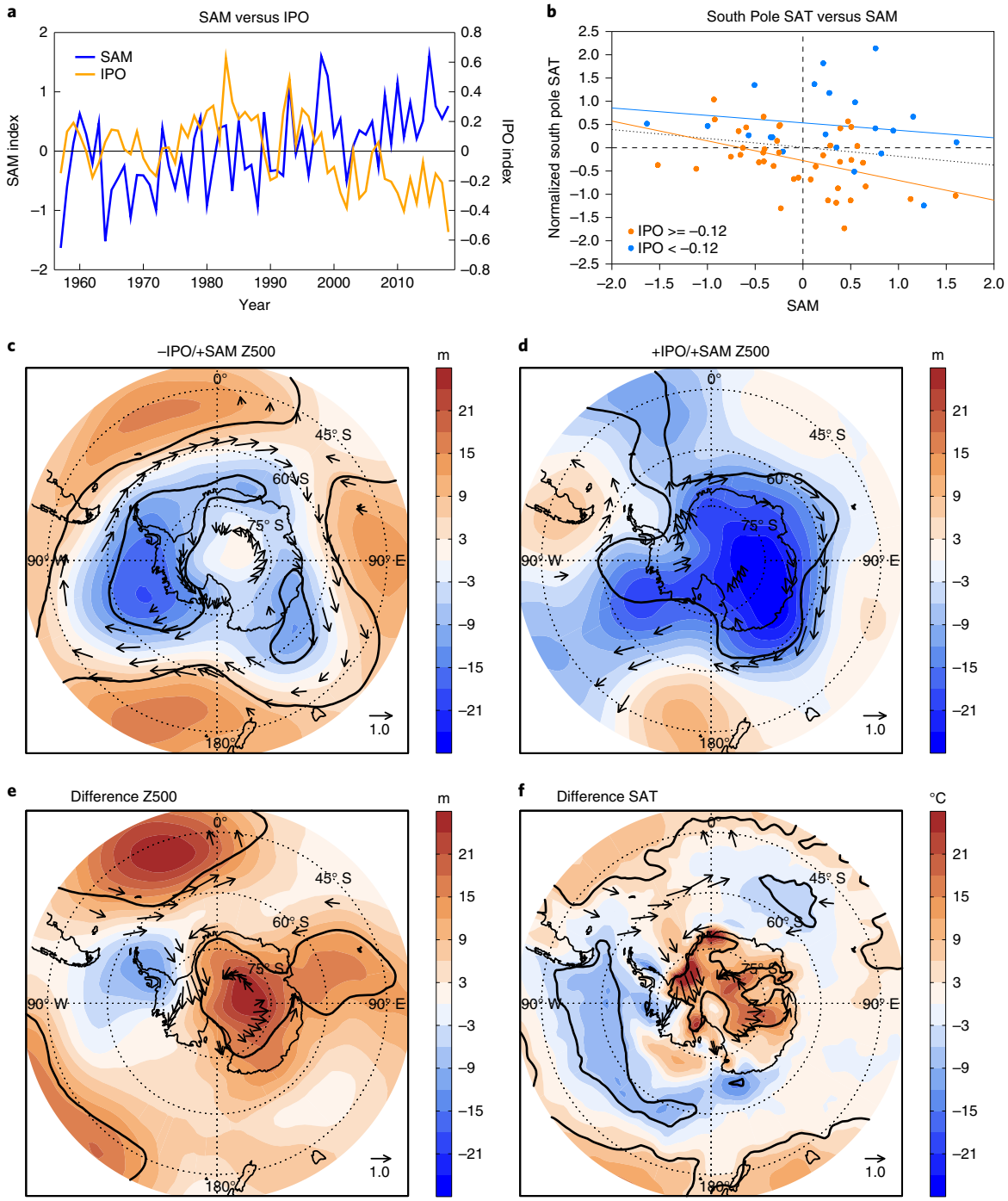

Fig. 5 | Coupling of IPO with positive SAM. a, The time series of the annual-mean SAM index (blue line; ref. [46]) and IPO residual index (orange line) over 1957–2018. **b**, Scatterplot of annual-mean SAM index versus the normalized South Pole SAT; years where IPO < −0.12 are plotted blue and all other years (IPO ≥ −0.12) are orange. The best-fit line for IPO < −0.12 yr and IPO ≥ −0.12 yr are shown as blue and orange lines, respectively. **c**,**d**, The annual-mean ERA5 Z500 (m) and 500 hPa wind (ms^{-1}) anomalies for positive SAM years that occurred with IPO < −0.12 (1999, 2001, 2004, 2005, 2008, 2009, 2010, 2011, 2012, 2013, 2015, 2016, 2017 and 2018) (**c**) and IPO > 0.12 (1979, 1983, 1985, 1993, 1995 and 1998) (**d**). **e**,**f**, The difference of +SAM/−IPO minus +SAM/+IPO groups; that is, **c** minus **d**, for ERA5 Z500 (m) (**e**) and ERA5 SAT (°C) and 500 hPa wind (ms^{-1}) (**f**). Black contours in **c**–**f** show where anomalies/differences are statistically significant at $P < 0.10$; only wind anomalies/differences significant at $P < 0.10$ are plotted.

Therefore we hypothesize that the cyclonic anomaly in the Weddell Sea was forced remotely via warming in the western equatorial Pacific due to the negative IPO trend. To test this, we performed a sensitivity experiment using an atmospheric model forced by a positive SST anomaly in the western equatorial Pacific (Fig. 4b; Methods). The SST anomaly produces a large-scale wave response over the South Pacific almost identical to the circulation pattern seen in the CMIP5 models with a negative SLP trend in the Weddell Sea (compare Fig. 4c,d), which results in a cyclonic anomaly in the Weddell Sea and associated warm northerly flow from the Weddell Sea into the continental interior (Fig. 4e,f).

The seasonal circulation and SAT anomalies induced by western tropical Pacific warming (Extended Data Figs. 5 and 6) shows statistically significant ($P<0.10$) northerly flow toward the South Pole and surface warming of the Antarctic interior in all seasons. However, the cyclonic anomaly in the Weddell Sea is most marked in the autumn and spring seasons, when the observed South Pole warming was also strongest (Fig. 1c). During autumn and spring, a wave train from the tropics is very pronounced (Extended Data Fig. 5), while during summer the warm northerly flow is tied more to anticyclonic anomalies over East Antarctica as conditions are unfavourable for wave propagation from the tropics into the high southern latitudes during this season[41]. During winter, the high-latitude cyclonic anomaly is located farther west in the South Pacific, which shifts the warm northerly flow toward the Antarctic Peninsula and possibly explains the absence of statistically significant South Pole warming in winter.

The role of positive SAM

There was also an exceptionally strong positive trend in the SAM during the recent South Pole warming period (Fig. 3a). The 2000s and 2010s are the only decades since 1957 in which negative IPO conditions occurred with a period of predominantly positive SAM polarity (Fig. 5a). Before 2000, when the South Pole cooled (Fig. 1b,c), the IPO was predominantly positive and there was only one negative IPO/positive SAM combination year (1999); since 2000, there have been a total of 13 negative IPO/positive SAM combination years.

The distribution of South Pole SAT anomalies by SAM polarity during the period 1957–2018 are shown in Fig. 5b. SAM events that occurred with IPO phases less than −0.12 (representing the lowest third of IPO values) are shown in blue and with other IPO phases (≥−0.12) are shown in orange. Interestingly, both the highest and lowest South Pole SATs are associated with positive SAM. The latter is expected given the usual spatial SAM–temperature relationship across Antarctica[22,24], while the former is associated with strongly negative IPO conditions (Fig. 5b; 69% of top right quadrant are blue dots). Furthermore, strongly negative IPO is almost always associated with positive SAT anomalies at the South Pole, regardless of the SAM polarity. The regression coefficient between the SAM and South Pole SAT using all 62 yr (black dotted line) and negative IPO years (blue line) are of similar slope (compare Fig. 5b), therefore for a given SAM value, South Pole SAT is typically ~0.5 °C warmer when combined with a strongly negative IPO. This implies negative IPO/western tropical Pacific warming is the primary driver of the South Pole warming but as shown next coupling of negative IPO with positive SAM may have contributed to the especially large warming in recent decades.

The circulation pattern for positive SAM events that occur with negative IPO (IPO < −0.12) versus positive IPO (IPO > 0.12) is shown in Fig. 5c,d. When positive SAM occurs with negative IPO, the Amundsen Sea Low node of the zonal wave three pattern[42] occurs further to the east in the western Weddell Sea, rather than over the Bellingshausen Sea, consistent with previous findings[43]. Differences between negative IPO coupling compared to positive IPO (Fig. 5e,f) demonstrate that negative IPO decreases pressure over the Bellingshausen Sea and western Weddell Sea and increases pressure over the Antarctic interior, producing anomalous northwesterly flow and positive SAT anomalies of 0.5–1 °C throughout the continental interior, both significant at $P<0.10$.

The CMIP5 pre-industrial runs reproduce this important coupling of negative IPO with positive SAM that contributed to the recent South Pole warming (Extended Data Fig. 7). Firstly, for 30-yr periods of strong negative IPO trends, the CMIP5 models reproduce the large-scale wave train pattern that is linearly congruent with the recent negative IPO trend (compare Extended Data Fig. 7a and Fig. 4h), including a broad pressure decrease over the high-latitude South Pacific extending into the Weddell Sea. Looking at 30-yr periods during which the models had an annual-mean positive SAM trend that matched the observed 1989–2018 annual-mean positive SAM trend (Extended Data Fig. 7b,c; Methods), the models that randomly had a negative IPO trend during their positive SAM trend display stronger negative pressure trends over the Weddell Sea compared to those that had a positive IPO trend (Extended Data Fig. 7b), which produces a nearly identical SAT warming pattern across the Antarctic interior (Extended Data Fig. 7c) as the warming pattern simulated in the models during their highest South Pole warming periods (Fig. 3d).

Conclusions

These results, along with prior studies[9,11,44,45], underscore the important role of natural circulation variability, particularly from the tropics, in driving extreme climate anomalies in interior Antarctica. While radiative forcing from greenhouse gas increases probably intensified the recent South Pole warming, the observed trend remains within the upper bounds of natural variability inferred from unforced, pre-industrial simulations and can be explained via a strong cyclonic anomaly in the Weddell Sea resulting from coupling of negative IPO and positive SAM during the twenty-first century; ENSO variability has not played a notable role in the recent South Pole warming. When compared to the estimated 1989–2018 warming from the historical/RCP 8.5 ensemble mean (Extended Data Data Fig. 2), decadal variability exceeds the anthropogenic signal by a factor of three, further supporting our conclusions that extreme decadal variability has masked anthropogenic warming across interior Antarctica during the twenty-first century (compare Figure 1a). As such, regional atmospheric circulation changes along the Antarctic coast are clearly important mechanisms driving extreme, multi-decadal climate anomalies over the interior. These findings must be considered to accurately assess and attribute large or abrupt climate changes over the data-sparse Antarctic interior, for example when assessing historical and future climate model simulations or interpreting past change detected in ice cores and other proxies.

Online content

Any methods, additional references, Nature Research reporting summaries, source data, extended data, supplementary information, acknowledgements, peer review information; details of author contributions and competing interests; and statements of data and code availability are available at https://doi.org/10.1038/s41558-020-0815-z.

Received: 20 November 2019; Accepted: 14 May 2020;
Published online: 29 June 2020

References

1. Hansen, J., Ruedy, R., Sato, M. & Lo, K. Global surface temperature change. *Rev. Geophys.* **48**, RG4004 (2010).
2. Turner, J. et al. Antarctic climate change during the last 50 years. *Int. J. Climatol.* **25**, 279–294 (2005).
3. Jones, J. M. et al. Assessing recent trends in high-latitude Southern Hemisphere surface climate. *Nat. Clim. Change* **6**, 917–926 (2016).
4. Vaughan, D. G. et al. Climate change: devil in the detail. *Science* **293**, 1777–1779 (2001).
5. Vaughan, D. G. et al. Recent rapid regional climate warming on the Antarctic Peninsula. *Clim. Change* **60**, 243–274 (2003).
6. Steig, E. J. et al. Warming of the Antarctic ice-sheet surface since the 1957 International Geophysical Year. *Nature* **457**, 459–462 (2009).
7. Bromwich, D. H. et al. Central West Antarctica among the most rapidly warming regions on Earth. *Nat. Geosci.* **6**, 139–145 (2012).
8. Nicolas, J. P. & Bromwich, D. H. New reconstruction of Antarctic near-surface temperatures: multidecadal trends and reliability of global reanalyses. *J. Clim.* **27**, 8070–8093 (2014).
9. Turner, J. et al. Absence of twenty-first century warming on Antarctic Peninsula consistent with natural variability. *Nature* **535**, 411–415 (2016).
10. Oliva, M. et al. Recent regional climate cooling on the Antarctic Peninsula and associated impacts on the cryosphere. *Sci. Total Environ.* **580**, 210–223 (2017).

11. Clem, K. R., Lintner, B. R., Broccoli, A. J. & Miller, J. R. Role of the South Pacific convergence zone in West Antarctic decadal climate variability. *Geophys. Res. Lett.* **46**, 6900–6909 (2019).
12. Screen, J. A. & Simmonds, I. The central role of diminishing sea ice in recent Arctic temperature amplification. *Nature* **464**, 1334–1337 (2010).
13. Thompson, D. W. J. & Solomon, S. Interpretation of recent Southern Hemisphere climate change. *Science* **296**, 895–899 (2002).
14. Thompson, D. W. J. et al. Signatures of the Antarctic ozone hole in Southern Hemisphere surface climate change. *Nat. Geosci.* **4**, 741–749 (2011).
15. Chapman, W. L. & Walsh, J. E. A synthesis of Antarctic temperatures. *J. Clim.* **20**, 4096–4117 (2007).
16. Schneider, D. P. & Steig, E. J. Ice cores record significant 1940s Antarctic warmth related to tropical climate variability. *Proc. Natl Acad. Sci. USA* **105**, 12154–12158 (2008).
17. Ding, Q., Steig, E. J., Battisti, D. S. & Küttel, M. Winter warming in West Antarctica caused by central tropical Pacific warming. *Nat. Geosci.* **4**, 398–403 (2011).
18. Schneider, D. P., Deser, C. & Okumura, Y. An assessment and interpretation of the observed warming of West Antarctica in the austral spring. *Clim. Dynam.* **38**, 323–347 (2012).
19. Li, X., Holland, D. M., Gerber, E. P. & Yoo, C. Impacts of the north and tropical Atlantic Ocean on the Antarctic Peninsula and sea ice. *Nature* **505**, 538–542 (2014).
20. Simpkins, G. R., McGregor, S., Taschetto, A. S., Ciasto, L. M. & England, M. H. Tropical connections to climatic change in the extratropical Southern Hemisphere: the role of Atlantic SST trends. *J. Clim.* **27**, 4923–4936 (2014).
21. Clem, K. R. & Fogt, R. L. South Pacific circulation changes and their connection to the tropics and regional Antarctic warming in austral spring, 1979–2012: S. Pacific trends and tropical influence. *J. Geophys. Res. Atmospheres* **120**, 2773–2792 (2015).
22. van den Broeke, M. R. & van Lipzig, N. P. M. Factors controlling the near-surface wind field in Antarctica. *Mon. Weather Rev.* **131**, 733–743 (2003).
23. Van Den Broeke, M. R. & Van Lipzig, N. P. M. in *Antarctic Peninsula Climate Variability: Historical and Paleoenvironmental Perspectives* Vol. 79 (eds Domack, E. et al.) 43–58 (American Geophysical Union, 2003).
24. Marshall, G. J. Half-century seasonal relationships between the Southern Annular mode and Antarctic temperatures. *Int. J. Climatol.* **27**, 373–383 (2007).
25. Kwok, R. & Comiso, J. C. Spatial patterns of variability in Antarctic surface temperature: connections to the Southern Hemisphere Annular Mode and the Southern Oscillation. *Geophys. Res. Lett.* **29**, 50-1–50-4 (2002).
26. Gorodetskaya, I. V. et al. The role of atmospheric rivers in anomalous snow accumulation in East Antarctica. *Geophys. Res. Lett.* **41**, 6199–6206 (2014).
27. Nicolas, J. P. & Bromwich, D. H. Climate of west Antarctica and influence of marine air intrusions. *J. Clim.* **24**, 49–67 (2011).
28. Marshall, G. J. & Thompson, D. W. J. The signatures of large-scale patterns of atmospheric variability in Antarctic surface temperatures. *J. Geophys. Res. Atmospheres* **121**, 3276–3289 (2016).
29. Nicolas, J. P. et al. January 2016 extensive summer melt in West Antarctica favoured by strong El Niño. *Nat. Commun.* **8**, 15799 (2017).
30. Marshall, G. J., Thompson, D. W. J. & Broeke, M. R. The signature of Southern Hemisphere atmospheric circulation patterns in Antarctic precipitation. *Geophys. Res. Lett.* **44**, 11580–11589 (2017).
31. Wille, J. D. et al. West Antarctic surface melt triggered by atmospheric rivers. *Nat. Geosci.* **12**, 911–916 (2019).
32. Blunden, J. & Arndt, D. S. State of the climate in 2018. *Bull. Am. Meteorol. Soc.* **100**, Si-S306 (2019).
33. Gillett, N. P. & Thompson, D. W. Simulation of recent Southern Hemisphere climate change. *Science* **302**, 273–275 (2003).
34. Solomon, S. et al. Emergence of healing in the Antarctic ozone layer. *Science* **353**, 269–274 (2016).
35. Campbell, E. C. et al. Antarctic offshore polynyas linked to Southern Hemisphere climate anomalies. *Nature* **570**, 319–325 (2019).
36. Turner, J. et al. Unprecedented springtime retreat of Antarctic sea ice in 2016. *Geophys. Res. Lett.* **44**, 6868–6875 (2017).
37. Turner, J., Bracegirdle, T. J., Phillips, T., Marshall, G. J. & Hosking, J. S. An initial assessment of Antarctic sea ice extent in the CMIP5 models. *J. Clim.* **26**, 1473–1484 (2013).
38. Smith, K. L. & Polvani, L. M. Spatial patterns of recent Antarctic surface temperature trends and the importance of natural variability: lessons from multiple reconstructions and the CMIP5 models. *Clim. Dynam.* **48**, 2653–2670 (2017).
39. Yuan, X. ENSO-related impacts on Antarctic sea ice: a synthesis of phenomenon and mechanisms. *Antarct. Sci.* **16**, 415–425 (2004).
40. Lachlan-Cope, T. & Connolley, W. Teleconnections between the tropical Pacific and the Amundsen–Bellinghausens Sea: role of the El Niño/Southern Oscillation. *J. Geophys. Res. Atmospheres* **111**, D23101 (2006).
41. Scott Yiu, Y. Y. & Maycock, A. C. On the seasonality of the El Niño teleconnection to the Amundsen Sea region. *J. Clim.* **32**, 4829–4845 (2019).
42. Raphael, M. N. A zonal wave 3 index for the Southern Hemisphere. *Geophys. Res. Lett.* **31**, L23212 (2004).
43. Marshall, G. J., Di Battista, S., Naik, S. S. & Thamban, M. Analysis of a regional change in the sign of the SAM–temperature relationship in Antarctica. *Clim. Dynam.* **36**, 277–287 (2011).
44. Trenberth, K. E., Fasullo, J. T., Branstator, G. & Phillips, A. S. Seasonal aspects of the recent pause in surface warming. *Nat. Clim. Change* **4**, 911–916 (2014).
45. Meehl, G. A., Arblaster, J. M., Bitz, C. M., Chung, C. T. Y. & Teng, H. Antarctic sea-ice expansion between 2000 and 2014 driven by tropical Pacific decadal climate variability. *Nat. Geosci.* **9**, 590–595 (2016).
46. Marshall, G. J. Trends in the Southern Annular Mode from observations and reanalyses. *J. Clim.* **16**, 4134–4143 (2003).

Methods

Data. We use observed monthly mean SAT data and upper-air radiosonde data from the Amundsen–Scott (South Pole) station and observed monthly mean SAT data from 19 other Antarctic staffed and automated weather stations. All observed data were obtained from the Scientific Committee on Antarctic Research (SCAR) Reference Antarctic Data for Environmental Research (READER) database[47]. Monthly mean surface values are calculated based on the synoptic (6-hourly) observations and only months with at least 90% of the 6-hourly observations were included in the analysis. We use the full SAT record for each station ending in 2018; the South Pole record spans the period 1957–2018 and contains 100% of the monthly mean SAT data. Radiosonde data (temperature and geopotential heights) at the South Pole, beginning in 1961, are based on 00Z and 12Z soundings during austral summer (primarily October–February) and 00Z soundings only primarily March–October; the radiosonde record is >80% complete, although there is a relaxed requirement for the number of daily observations per month compared to surface data in the READER archive. Furthermore, due to its high elevation, radiosonde data are only available at or above 500 hPa at the South Pole. We also analyse 6-hourly wind observations at the South Pole, also obtained from the SCAR READER database[47]. There are 225,154 valid winds spanning the period 1957–2019 with the frequency changing from 6-hourly in the early years to hourly from 2001. However, for consistency we only use the 6-hourly observations which reduces the sample size to 90,955 wind observations. Due to its location, wind direction at the South Pole is based on the geographic longitudinal grid, with grid northerly winds coming from 0°, grid easterly coming from 90° E, grid southerly coming from 180° and grid westerly coming from 90° W.

To investigate atmospheric circulation during 1979–2018, we use monthly mean atmospheric fields from ERA5, the fifth global reanalysis produced by the European Centre for Medium-Range Weather Forecasts[48] interpolated to a 1.5° × 1.5° grid spacing. We investigate monthly mean SSTs using the National Oceanic and Atmospheric Administration (NOAA) extended reconstructed SST (ERSSTv.5; ref. [49]) dataset, which has a 2° × 2° grid spacing. Changes in tropical deep convection are investigated using monthly mean interpolated outgoing longwave radiation (OLR)[50] data obtained from NOAA's Physical Sciences Division, which have a 2.5° × 2.5° grid spacing.

To place the recent South Pole SAT trends in context with all possible ranges of natural (unforced) and anthropogenically forced variability, we use the CMIP5 (ref. [51]) pre-industrial control, historical and RCP 8.5 climate model simulations interpolated to a 2° × 2° grid resolution. All simulations are fully coupled (ocean–atmosphere). The pre-industrial control simulations are integrated for hundreds of years with prescribed greenhouse gas and stratospheric ozone concentrations that are representative of pre-industrial conditions, thereby reflecting natural, unforced variability in the climate system. The historical and RCP 8.5 simulations are free-running (that is, natural, internal variability in the climate system is generated by the model) but time-varying greenhouse gas and stratospheric ozone concentrations are prescribed based on observed values since 1850. We use all available models and their ensemble members with SAT output to compare with the recent observed 1989–2018 South Pole SAT, which equates to a total of 52 pre-industrial runs, 209 historical runs and 107 RCP 8.5 runs; the 209 historical runs span the period 1850–2005 and we use the 107 RCP 8.5 runs for the period 2006–2018. Because the historical/RCP 8.5 simulations generate their own internal variability, we average across all models/ensemble members to remove internal variability and isolate the externally forced signal arising from natural (for example, volcano eruptions) and anthropogenic (for example, increasing greenhouse gas concentrations) climate forcing. The multi-model mean running 30-yr South Pole SAT trends are shown in Extended Data Fig. 2, which estimates the annual-mean anthropogenic warming to be 0.98 °C during the 1989–2018 period.

We compare the observed 1989–2018 South Pole warming trend to all possible 30-yr South Pole SAT trends simulated within the models by calculating every possible 30-yr annual-mean South Pole SAT trend for each model/ensemble member, which equates to 25,785 30-yr trends for the pre-industrial runs and 25,503 30-yr trends for the merged historical/RCP 8.5 runs. Next, we compare the observed 1989–2018 trend to only the highest 30-yr warming trend simulated by each ensemble member, that is 52 trends in the pre-industrial ensemble and 209 trends in the historical/RCP 8.5 ensemble.

We found that the largest warming trends in both ensembles were heavily skewed by the GISS model, as all ten (19%) and all 46 (21%) of the highest pre-industrial and historical/RCP 8.5 SAT trends, respectively, were comprised of the GISS runs/ensemble members. The magnitude of the GISS warming trends are extremely large, ranging from 4.2 to 8.7 °C 30-yr^{-1}, more than three times larger than the models with the second highest warming and nearly five times larger than the observed 1989–2018 warming. This large warming in the GISS simulations appears due in part to a much larger simulated interannual variability of SAT at the South Pole compared to other models and observations. Therefore it is more appropriate to compare the magnitude of the observed and simulated 30-year trends using normalized South Pole SAT data, which effectively removes the trend biases due to variations in the magnitude of internal variability. We normalize the observed and simulated South Pole SAT using the long-term mean and standard deviation over the full 1957–2018 South Pole record and the full SAT record in each ensemble member, respectively. To examine the large-scale SST and SLP patterns, we use the 52 pre-industrial runs only, as these simulations cover a longer time span than the historical simulations and reflect natural climate fluctuations that are not influenced by external anthropogenic forcing.

We investigate the IPO in both the models and observations using the unfiltered tripole index[52], which is the difference between the SST anomaly averaged over the central equatorial Pacific (10° S–10° N, 170° E–90° W) minus the SST anomaly averaged over the extra-tropical North (25° N–45° N, 140° E–145° W) and South (50° S–15° S, 150° E–160° W) Pacific. However, due to the strong interannual covariability of the tripole index with variability in ENSO (that is, annual-mean correlation >0.90), we linearly remove covariability with Niño 3.4 SSTs from the IPO index using a linear least squares regression approach. We subtract the predicted IPO value obtained from the regression analysis from the original IPO index and use the remaining residual for analysis, termed the IPO residual index. This approach ensures the IPO residual index has a zero correlation with the Niño 3.4 SSTs and benefits by capturing more low-frequency SST variability that occurs outside of the central equatorial Pacific[53]. We follow the same methodology for calculating the IPO residual index in the CMIP5 pre-industrial SST fields. ENSO variability is examined separately using the Niño 3.4 SST anomaly obtained from NOAA's Climate Prediction Center, which is the average SST anomaly in the region 5° S–5° N, 170–120° W; the same methodology is used for calculating the Niño 3.4 SST anomaly in the CMIP5 models, which is used to calculate the IPO residual index.

We examine the pre-industrial ensemble mean 30-yr annual-mean SLP trend for the lowest 30-yr negative IPO trend periods in Extended Data Fig. 7a. We find many models show a broad SST cooling bias over the western equatorial and tropical South Pacific that extends from South America all the way to Papua New Guinea (~150° E). Therefore we include only the models that simulate a realistic negative IPO pattern, as shown in Fig. 4g, with a positive SST trend in the western equatorial Pacific (10° N–10° S, 150–165° E) and a negative SST trend in the eastern tropical South Pacific (5–15° S, 120–90° W).

Unless otherwise stated, variability in the SAM is investigated using the difference in normalized zonal-mean SLP between 40° S and 65° S (ref. [54]). This approach allows for a comparison of the observationally-constrained 1989–2018 SAM index trend (based on ERA5 SLP data) and the SAM index trends in the models (based on model SLP data). However, in Fig. 5 we use the observation-based index of Marshall[46], which begins in 1957 and therefore allows an analysis of SAM relationships with South Pole SAT and the IPO over the full 1957–2018 period.

In Extended Data Figs. 7b,c we calculate all possible 30-yr annual-mean SAM trends for each pre-industrial ensemble member and retain the 30-yr periods for which the SAM trend matched the observed 1989–2018 SAM trend (0.71 decade^{-1} or 2.14 30-yr^{-1}). From these positive SAM trends, next we grouped the models that randomly had a negative IPO trend (and a positive SST trend in the western equatorial Pacific) and subtracted from the group of models that randomly had a positive IPO trend (and a negative SST trend in the western equatorial Pacific) to see if negative IPO/positive SAM coupling results in a negative pressure trend in the Weddell Sea, as seen in observations.

Annual-means are calculated over the 12 calendar months January–December. Seasonal means are the 3-month averages with respect to the Southern Hemisphere: austral autumn is March–April–May (MAM), austral winter is June–July–August (JJA), austral spring is September–October–November (SON) and austral summer is December–January–February (DJF). The DJF season corresponds to the December year, that is DJF 1957 ends in February 1958 and DJF 2018 ends in February 2019.

Model experiment. We performed two experiments using the National Center for Atmospheric Research Community Earth System Model v.1.2 (CESM1.2; ref. [55]). The model was run in atmosphere-only mode using Community Atmosphere Model 5 (CAM5) physics and dynamics at a horizontal resolution of 1.9° × 2.5° with 30 vertical levels. We prescribe pre-industrial concentrations of greenhouse gases and stratospheric ozone representative of the 1850s and climatological sea ice concentrations (1982–2001) and climatological SSTs (1950–2017). We perform two 30-yr simulations following a 1-yr spin-up: one control run with annually repeating monthly mean climatological SSTs and one perturbed run with a +2 °C SST anomaly imposed in the western equatorial Pacific at 2° S, 158° E. The SST anomaly is dampened to zero following a sine function moving away from the anomaly on all sides in a 10° × 10° box to avoid spurious SST gradients. The SST region used in the experiment is not correlated with ENSO: the detrended correlation of the west Pacific SST with Niño 3.4 is 0.07 (1957–2018) and 0.01 (1979–2018) and for the Southern Oscillation index the correlation is −0.07 (1957–2018) and 0.01 (1979–2018).

Statistical methods. Trends and regressions are calculated using the standard least squares linear regression approach. Statistical significance of trends/regressions are calculated following ref. [56] using a two-tailed Student's t-test with $n-2$ degrees of freedom (n being number of years) and a null hypothesis that the trend/regression is zero. We calculate the t ratio, which is the least squares linear regression estimate of the trend compared to the standard error of the trend, which we then compare to the critical t value for $n-2$ degrees of freedom following a Student's t distribution to obtain the confidence level P.

Linear congruency of the IPO residual with SST and SLP in Fig. 4g,h is calculated by first regressing the SST and SLP fields onto the IPO residual index and then multiplying the regression coefficient at every grid cell by the observed trend in the IPO residual index.

A single-mean composite anomaly is calculated for the IPO and SAM groups in Fig. 5c,d and a difference in two means is calculated in Fig. 5e,f and Extended Data Figs. 5 and 6 following previous work[56]. For the former, we average the anomaly from the 1981–2010 climatology for each group and, for the latter, we calculate the difference in the means of the two groups. We use a one-tailed single-mean Student's *t*-test with $n-1$ degrees of freedom for Fig. 5c,d, and a two-tailed difference in means *t*-test with $n+m-2$ degrees of freedom for Fig. 5e,f and Extended Data Figs. 5 and 6 (n and m being the number of years in each group, respectively). Both have a null hypothesis that the anomaly/difference is zero. The confidence level P is computed by comparing the standard error of the groups with the critical Student's t value.

Data availability

The station temperature, wind and radiosonde data are available online at https://legacy.bas.ac.uk/met/READER/. ERA5 data are available online at https://www.ecmwf.int/en/forecasts/datasets/reanalysis-datasets/era5. ERSSTv.5 and OLR data are available online at https://www.esrl.noaa.gov/psd/data/gridded/index.html. The CMIP5 data are available online at http://data.ceda.ac.uk/badc/cmip5. Output from the CESM experiments are available from the authors upon request.

Code availability

All code used to perform the calculations can be accessed at https://doi.org/10.5281/zenodo.3712453.

References

47. Turner, J. et al. The SCAR READER project: toward a high-quality database of mean Antarctic meteorological observations. *J. Clim.* **17**, 2890–2898 (2004).
48. Hersbach, H. et al. Global reanalysis: goodbye ERA-Interim, hello ERA5. *ECMWF Newsletter* **159**, 17–24 (2019).
49. Huang, B. et al. Extended Reconstructed Sea Surface Temperature, Version 5 (ERSSTv5): upgrades, validations, and intercomparisons. *J. Clim.* **30**, 8179–8205 (2017).
50. Liebmann, B. & Smith, C. A. Description of a complete (interpolated) outgoing longwave radiation dataset. *Bull. Am. Meteorol. Soc.* **77**, 1275–1277 (1996).
51. Taylor, K. E., Stouffer, R. J. & Meehl, G. A. An overview of CMIP5 and the experiment design. *Bull. Am. Meteorol. Soc.* **93**, 485–498 (2012).
52. Henley, B. J. et al. A tripole index for the Interdecadal Pacific Oscillation. *Clim. Dynam.* **45**, 3077–3090 (2015).
53. Folland, C. K., Parker, D. E., Colman, A. W. & Washington, R. in *Beyond El Niño* (Ed. Navarra, A.) 73–102 (Springer, 1999).
54. Gong, D. & Wang, S. Definition of Antarctic Oscillation index. *Geophys. Res. Lett.* **26**, 459–462 (1999).
55. Hurrell, J. W. et al. The Community Earth System Model: a framework for collaborative research. *Bull. Am. Meteorol. Soc.* **94**, 1339–1360 (2013).
56. Wilks, D. *Statistical Methods in the Atmospheric Sciences* Vol. 100 (Academic Press, 2005).

Acknowledgements

R.L.F. is grateful for funding from the National Science Foundation under grant no. US NSF PLR-1744998. J.T. and G.J.M. were supported by the UK Natural Environment Research Council through the British Antarctic Survey research programme Polar Science for Planet Earth. We thank the Rutgers Office of Advanced Research Computing and G. Collier for assistance with the CESM simulations. We thank A. Orr and A. Moody for valuable discussion during this study. We acknowledge the World Climate Research Programme's Working Group on Coupled Modelling, which is responsible for CMIP, and we thank the climate modelling groups for producing and making available their model output. For CMIP the US Department of Energy's Program for Climate Model Diagnosis and Intercomparison provides coordinating support and led development of software infrastructure in partnership with the Global Organization for Earth System Science Portals.

Author contributions

K.R.C. and R.L.F. conceived the study. K.R.C. led the writing of the manuscript, carried out the South Pole SAT and ERA5 circulation analysis, analysed the CMIP5 data and performed the CESM experiments. R.L.F. investigated changes in upper-air temperature and pressure from South Pole radiosonde observations and generated Fig. 1. J.T. investigated changes in South Pole winds using South Pole wind observations and generated Fig. 2c–e. G.J.M. investigated IPO/SAM influence on South Pole temperatures and generated Fig. 5. K.R.C. generated all other figures. All authors analysed the results and assisted in writing and editing the manuscript.

Competing interests

The authors declare no competing interests.

Additional information

Extended data is available for this paper at https://doi.org/10.1038/s41558-020-0815-z.

Correspondence and requests for materials should be addressed to K.R.C.

Peer review information: *Nature Climate Change* thanks Sharon Stammerjohn, Xiaojun Yuan and the other, anonymous, reviewer(s) for their contribution to the peer review of this work.

Reprints and permissions information is available at www.nature.com/reprints.

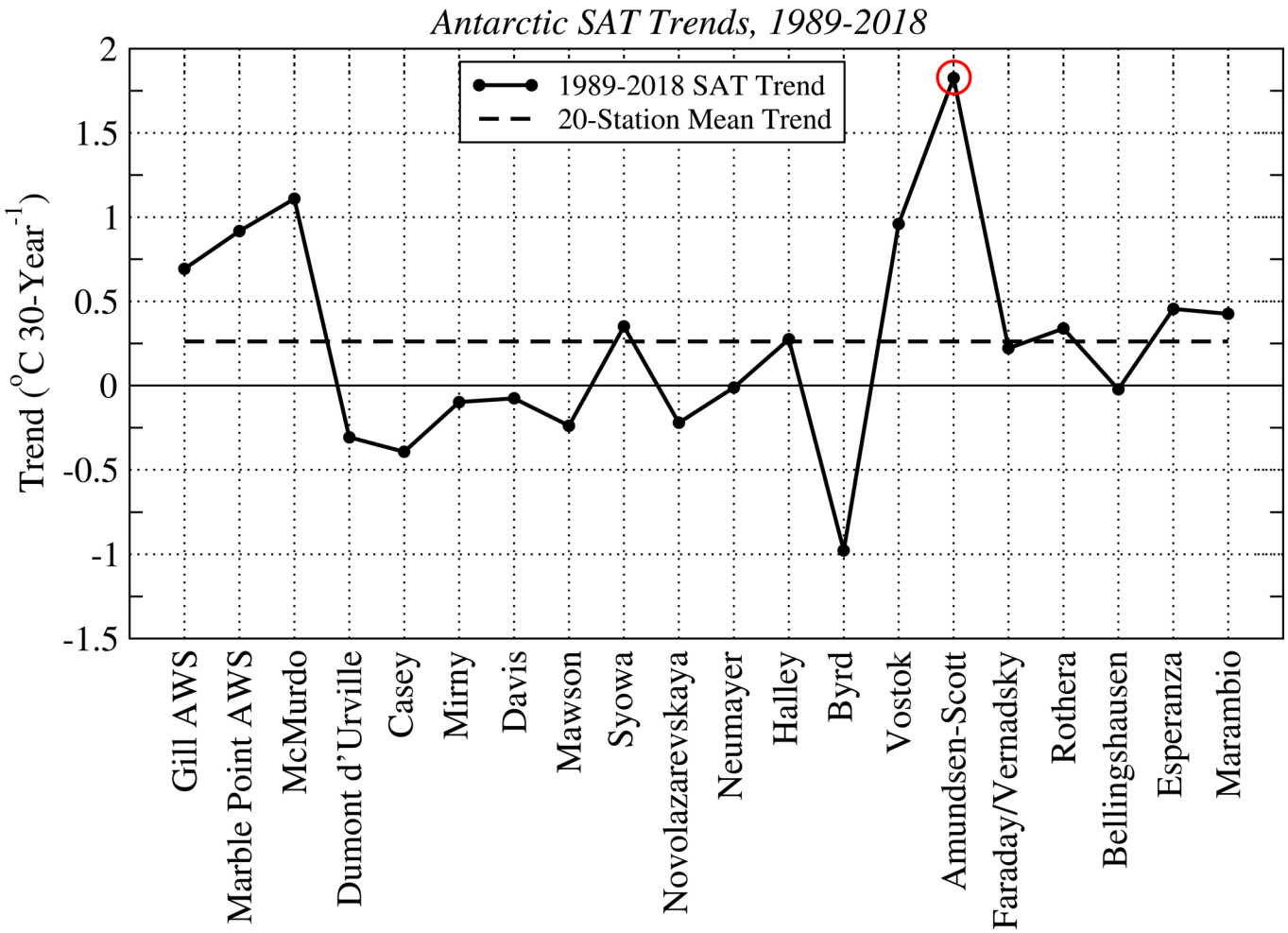

Extended Data Fig. 1 | Antarctic SAT trends during 1989–2018. Observed 1989–2018 annual-mean SAT trends (°C 30-year^{-1}) from 20 Antarctic staffed and automated weather stations (solid line). The mean trend for all 20 stations is 0.26 °C 30-year^{-1} and is denoted by the dashed line. The Amundsen–Scott warming trend of 1.83 °C 30-year^{-1} is denoted by an open red circle.

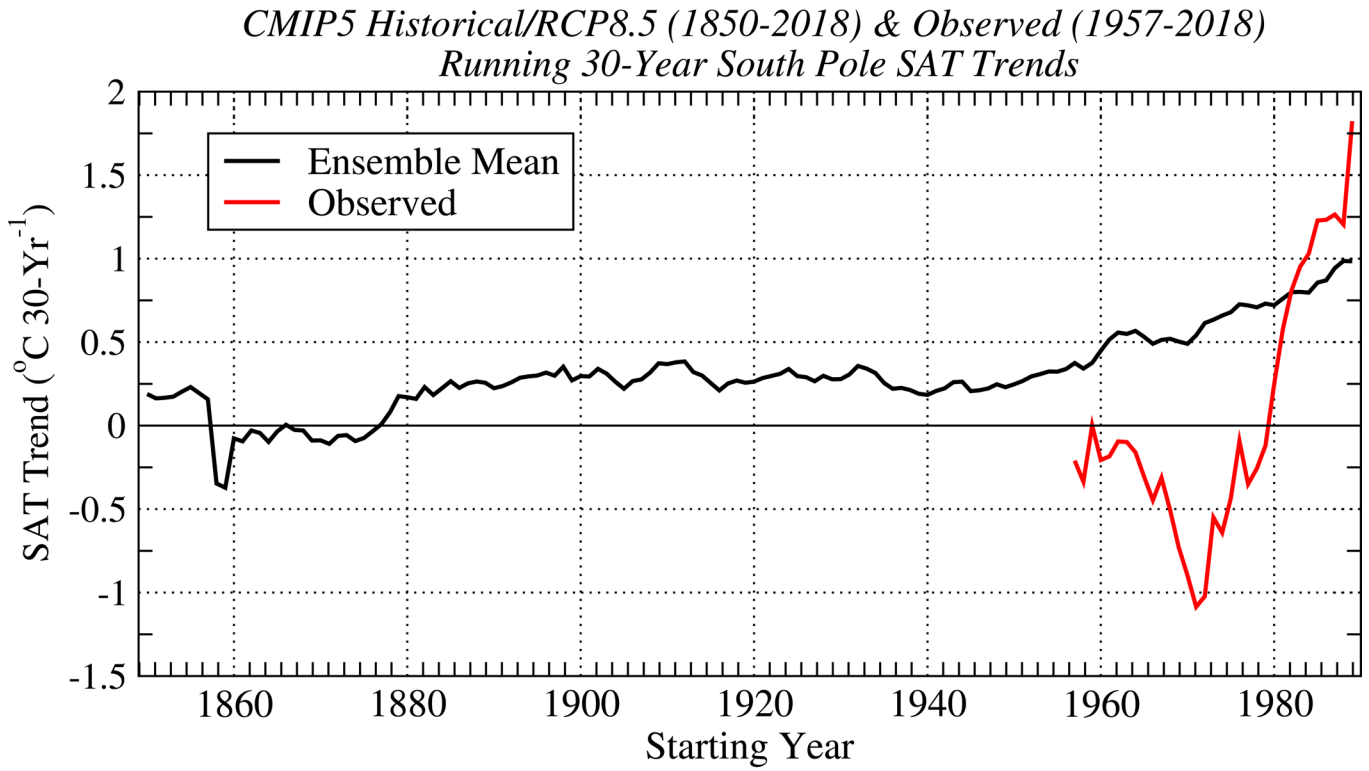

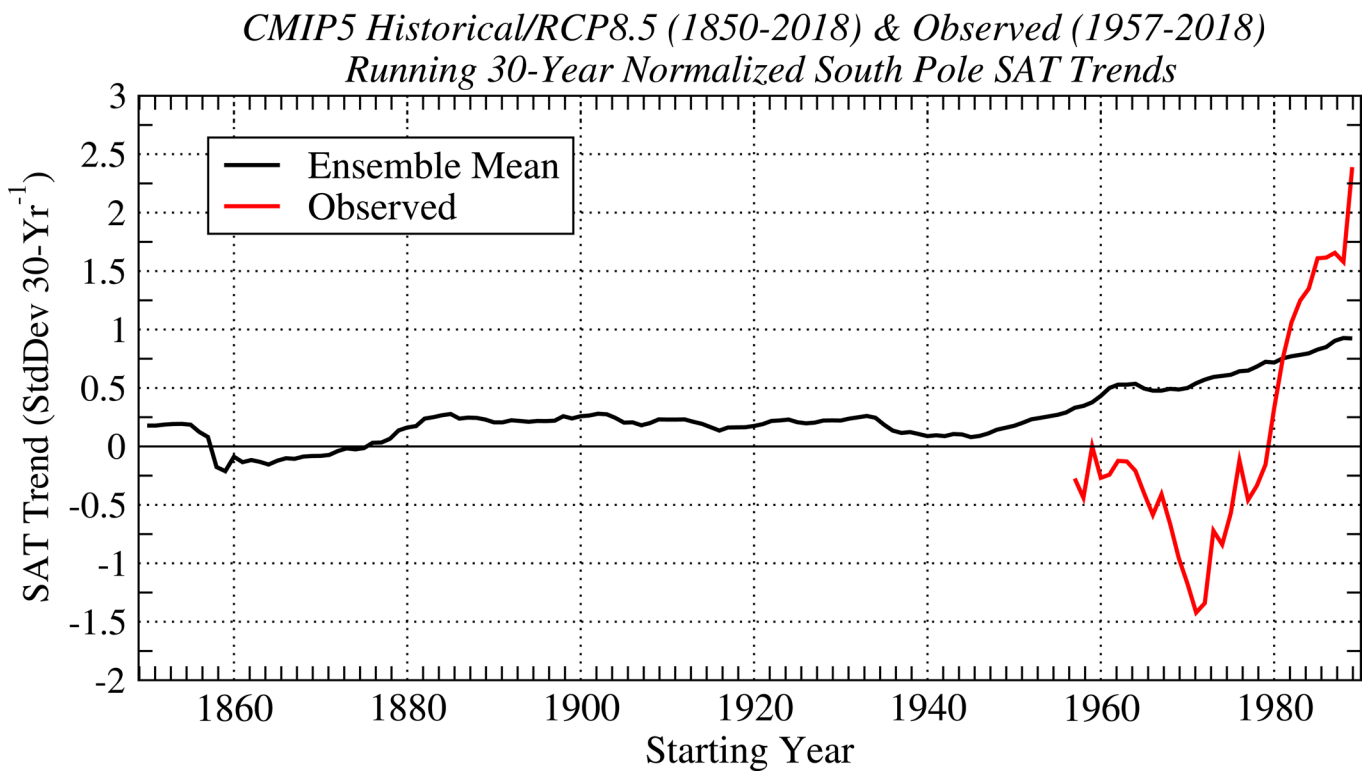

Extended Data Fig. 2 | Simulated anthropogenic forcing of South Pole surface air temperature in CMIP5 models. Running 30-year South Pole annual-mean (a) SAT and (b) normalized SAT trends for the merged historical (1850–2005) and RCP8.5 (2006–2018) ensemble mean (black line) compared to the observed Amundsen–Scott SAT running 30-year trends (red line). The ensemble mean SAT trend for 1989–2018 is 0.98 °C 30-year^{-1} (54% of the observed 1.83 °C 30-year^{-1}) and the ensemble mean normalized SAT trend is 0.92 standard deviations 30-year^{-1} (39% of the observed 2.39 standard deviations 30-year^{-1}).

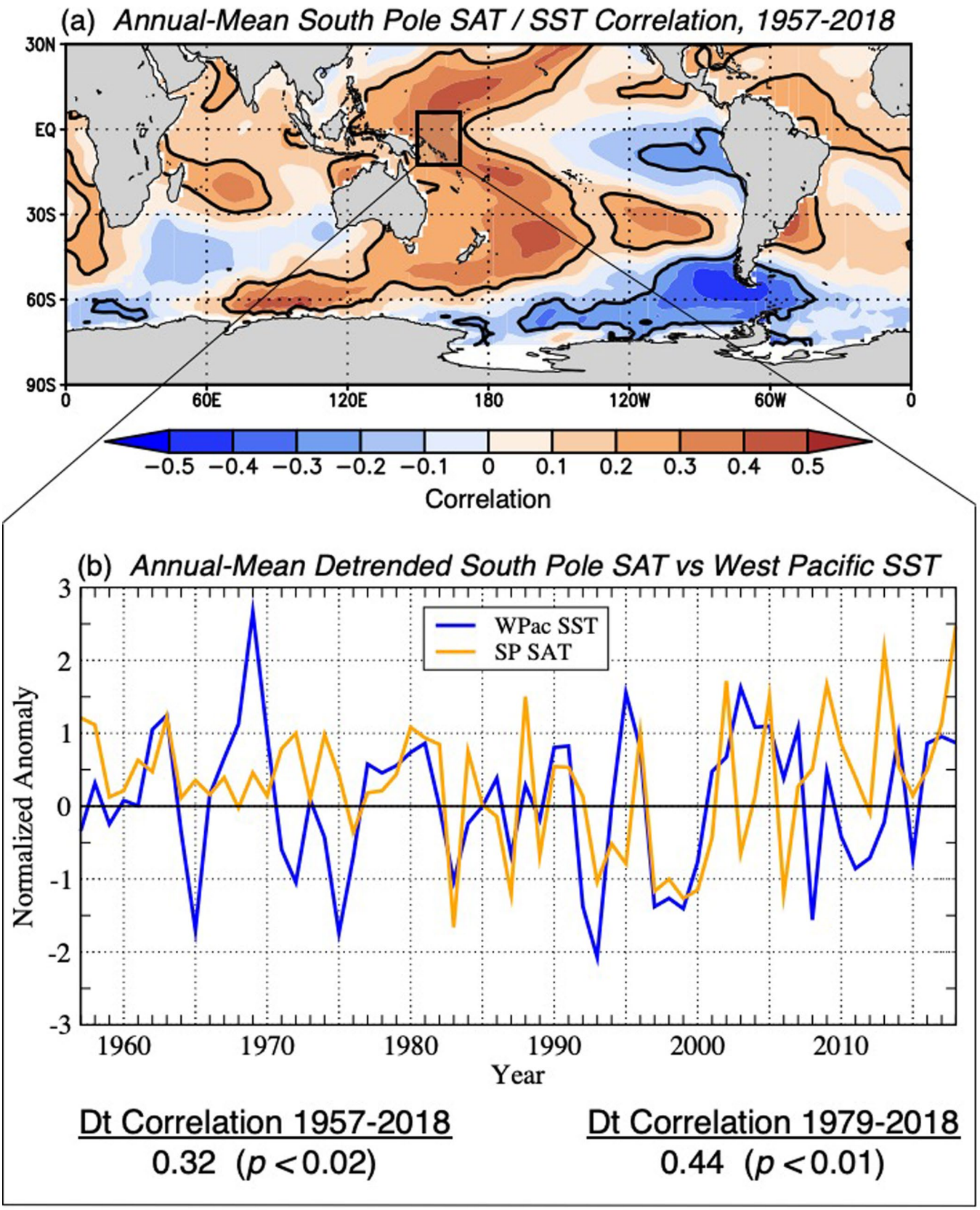

Extended Data Fig. 3 | South Pole relationship with tropical sea surface temperatures. The (a) correlation of annual-mean Amundsen–Scott SAT with ERSSTv5 SST over the period 1957–2018, and (b) the detrended time series of annual-mean Amundsen–Scott SAT and annual-mean SST in the western tropical Pacific region used for the sensitivity experiment (148–168°E, 8°N-12°S). The black contours in (a) show correlations significant at $p<0.10$. The detrended correlations of annual-mean Amundsen–Scott SAT and west Pacific SST and the statistical significance for the 1957–2018 and 1979–2018 periods are given at the bottom.

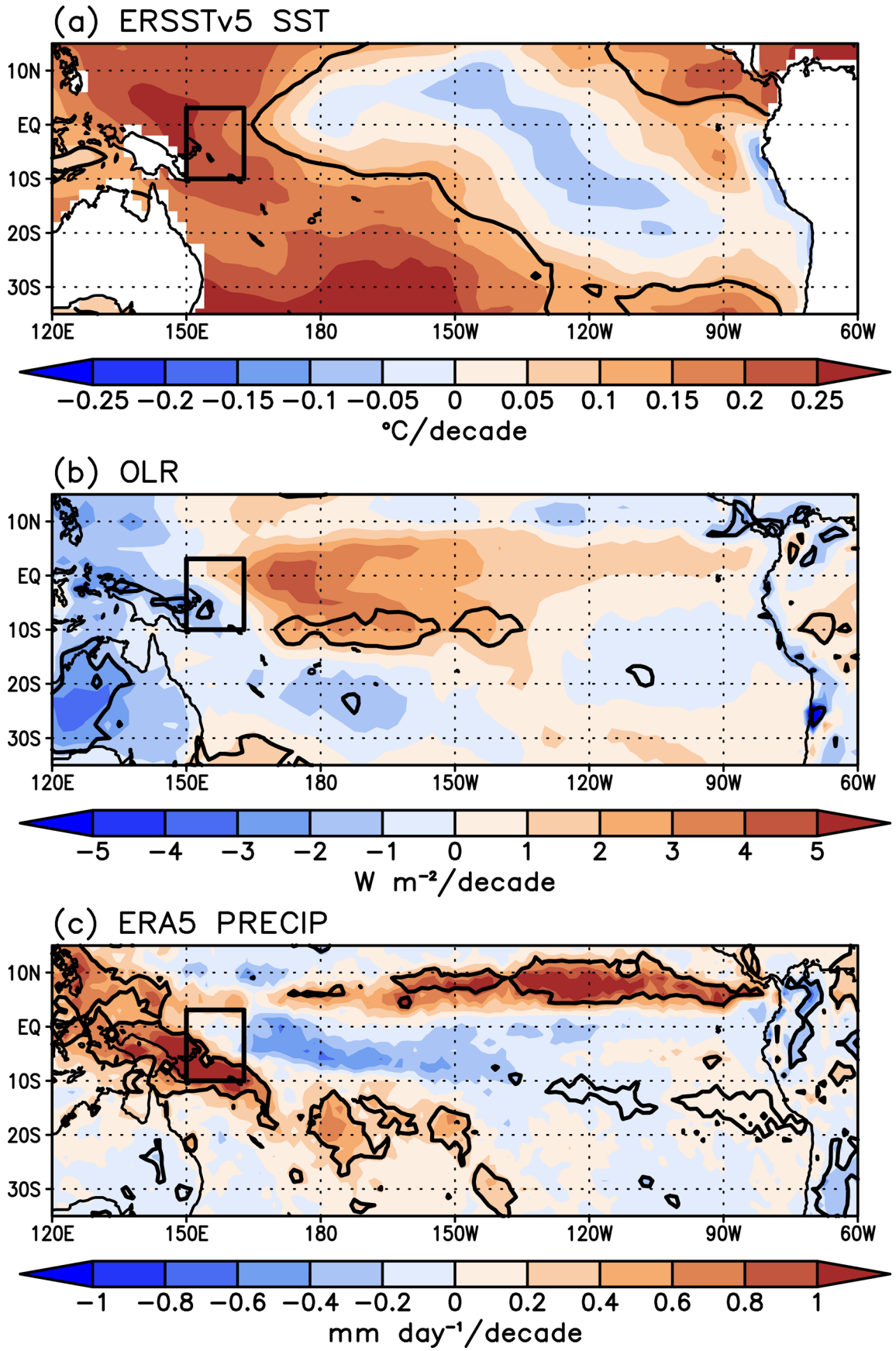

Extended Data Fig. 4 | Tropical Pacific climate trends during 1989–2018. The 1989–2018 annual-mean trends in (a) tropical SST (°C decade^{-1}), (b) outgoing longwave radiation (W m^{-2} decade^{-1}), and (c) ERA5 precipitation (mm day^{-1} decade^{-1}). The black box in (a–c) denotes the region where the positive SST anomaly was placed for the sensitivity experiment. Black contours denote trends that are significant at $p<0.10$.

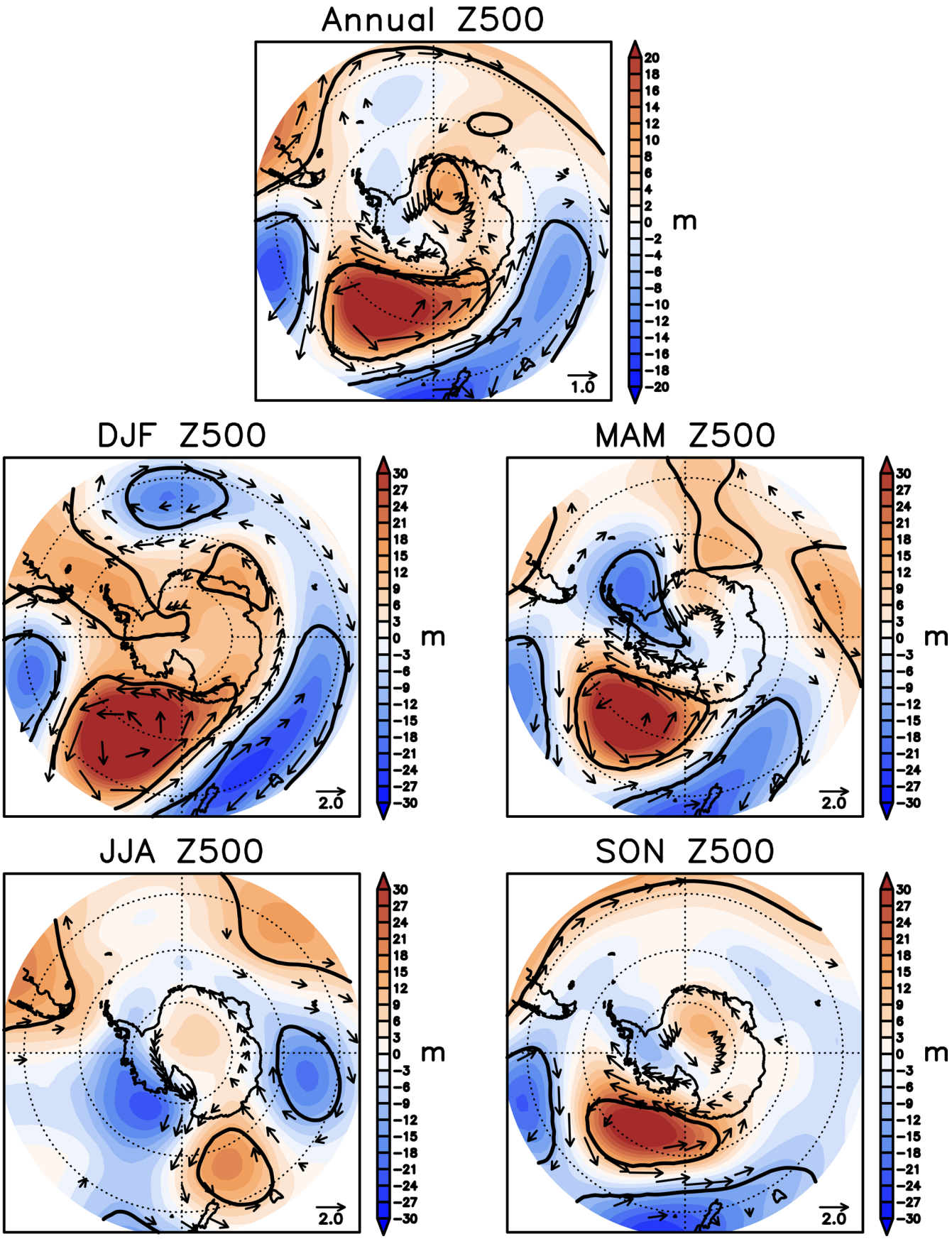

Extended Data Fig. 5 | Simulated Antarctic circulation response to western tropical Pacific warming. The annual and seasonal-mean Z500 (m) and 500 hPa wind (ms^{-1}) anomalies (perturbed run 30-yr climatology minus control run 30-yr climatology) for the west Pacific SST heating anomaly experiment (Methods). Black contours denote Z500 anomalies significant at $p<0.10$, and only wind anomalies significant at $p<0.10$ are plotted.

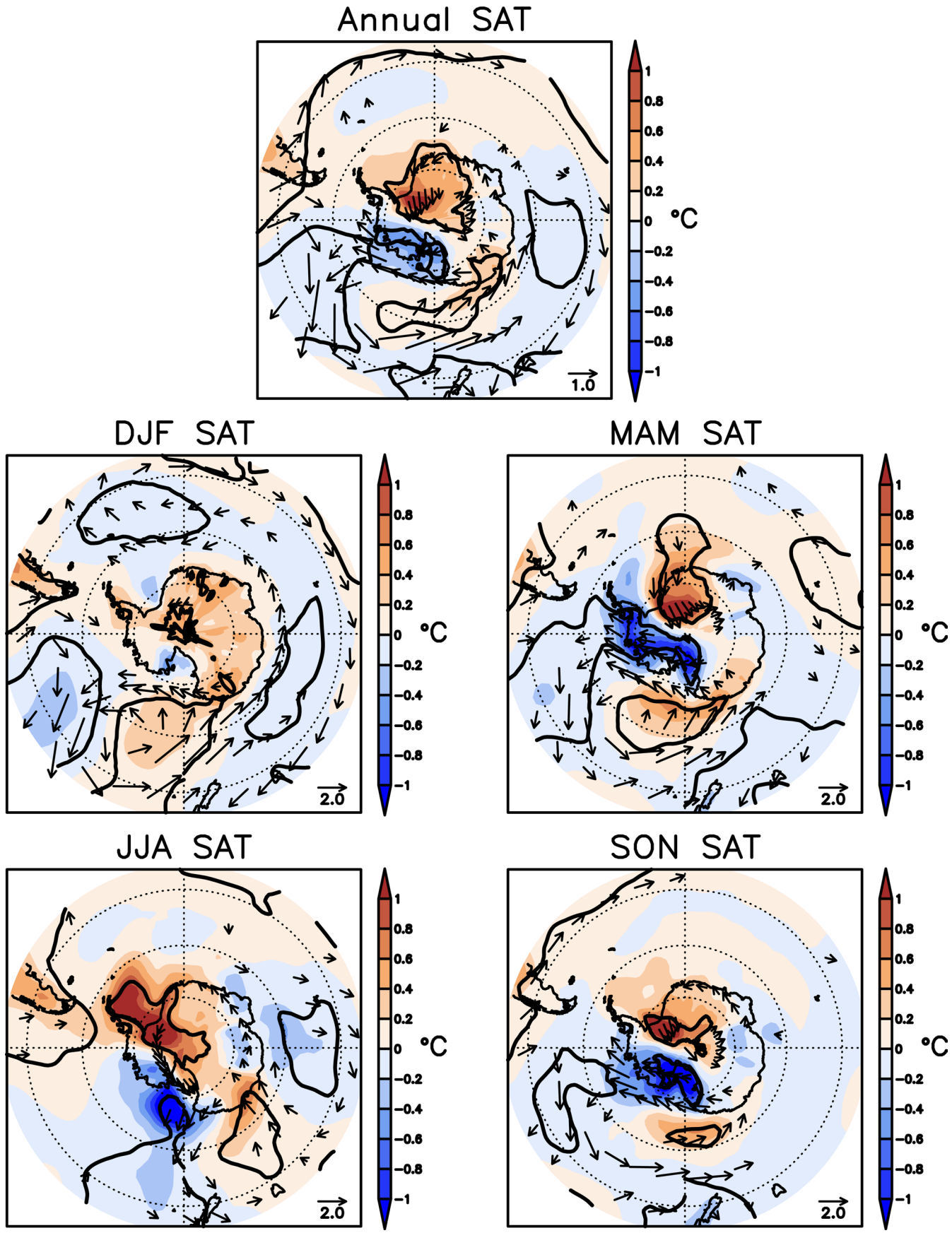

Extended Data Figure 6 | Simulated Antarctic surface air temperature response to western tropical Pacific warming. As in Extended Data Fig. 5, except for SAT (°C).

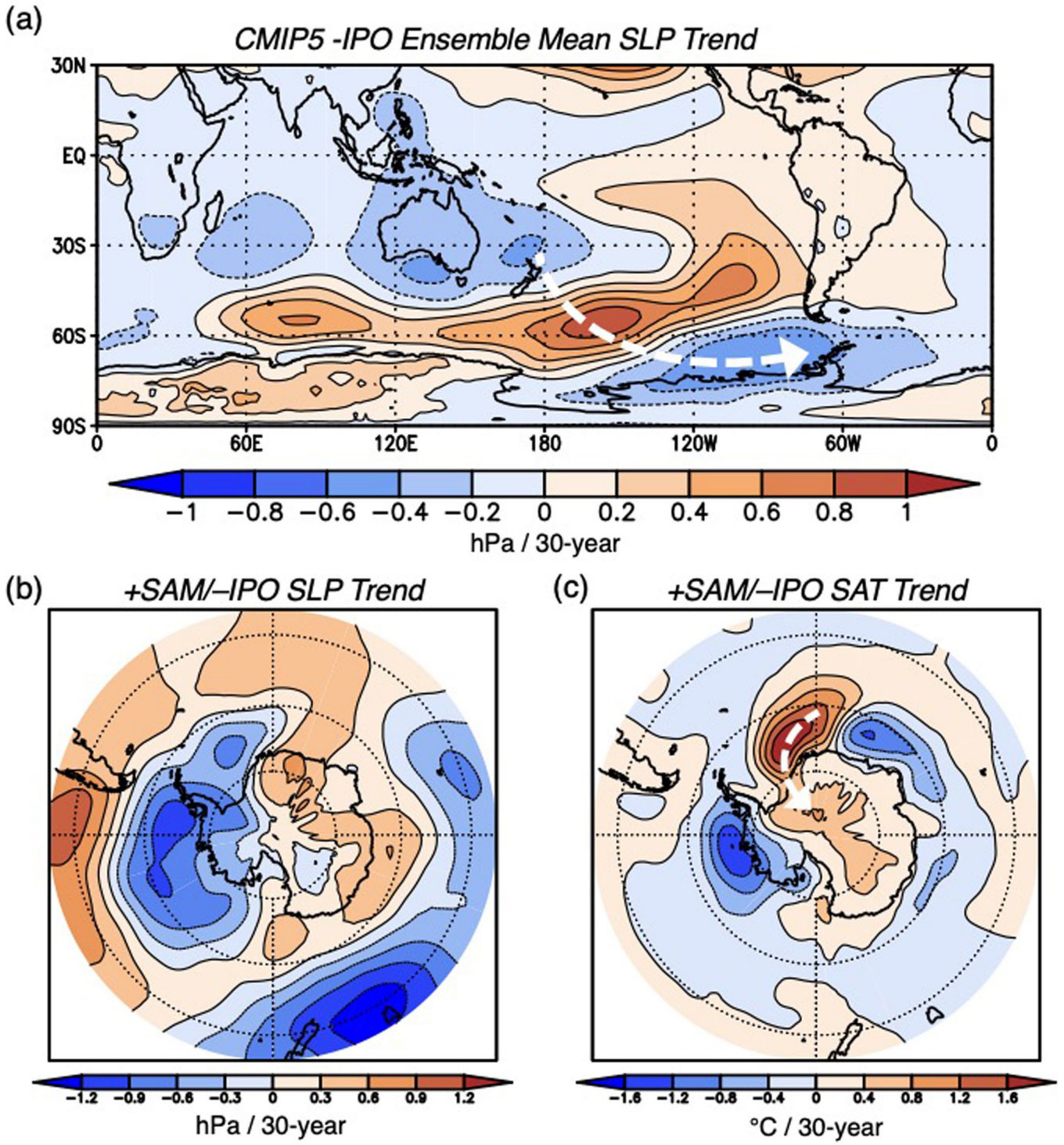

Extended Data Figure 7 | The influence of negative IPO and positive SAM coupling on Antarctic climate in CMIP5 models. The (a) CMIP5 pre-industrial ensemble mean annual-mean 30-year SLP trend (hPa 30-year^{-1}) for the lowest 30-year negative IPO trend period in each ensemble member. Only CMIP5 models that simulate a realistic negative IPO SST pattern (a positive SST trend in the western tropical Pacific and a negative SST trend in the southeastern tropical Pacific) were included (Methods). (b-c) The difference in annual-mean 30-year (b) SLP (hPa 30-year^{-1}) and (c) SAT (°C 30-year^{-1}) trend for CMIP5 pre-industrial models that had a negative IPO trend minus those that had a positive IPO trend during their respective 30-year period with a positive SAM trend equal to the observed 1989–2018 positive SAM trend (2.14 30-year^{-1}).